Rotational Contour Analysis of Jet-Cooled Methyl Hydroperoxide Action Spectra in the Region of the $2\nu_{OH}$ and $3\nu_{OH}$ Bands[†]

Jamie Matthews and Amitabha Sinha*

Department of Chemistry and Biochemistry, University of California—San Diego,
9500 Gilman Drive, La Jolla, California 92093-0314

Received: March 10, 2009; Revised Manuscript Received: June 10, 2009

State-selected photodissociation is used to record the partially rotationally resolved action spectra of CH_3OOH in the region of its first and second OH-stretching overtones ($2\nu_{OH}$ and $3\nu_{OH}$) under free-jet expansion conditions. From an analysis of the rotational band contours for the OH-stretching states and their corresponding COOH torsion combination bands, effective rotational constants and transition dipole moment orientations are determined for the vibrational eigenstates. The level splitting between the lowest symmetric and antisymmetric pair of COOH torsion levels, 0^+ and 0^-, associated with the $2\nu_{OH}$ overtone state is found to be ~ 3.9 cm^{-1}. Comparison of spectra in the region of the $2\nu_{OH}$ and $2\nu_{OH} + \nu_{COOH}$ bands in CH_3OOH and CD_3OOH reveals that the spectral features in CH_3OOH are substantially more perturbed compared to those of its deuterated counterpart, suggesting that modes involving the methyl rotor contribute significantly to promoting intramolecular vibrational energy redistribution (IVR) in CH_3OOH. Furthermore, a comparison of the average rotational line widths in both CH_3OOH and CD_3OOH for the $2\nu_{OH}$ and $2\nu_{OH} + \nu_{COOH}$ bands appears to suggest that at these energies, adding one quanta of low-frequency COOH torsional motion does not enhance the IVR rate relative to that of the pure OH-stretching overtone.

I. Introduction

Methyl hydroperoxide (CH_3OOH; MHP) is an atmospherically important molecule as it is a source of OH radicals.[1−3] It is also the smallest organic hydroperoxide (R−OOH) and, as such, serves as a prototype for investigating the dissociation dynamics and vibrational spectroscopy of larger organic hydroperoxides. The electronic ground state of methyl hydroperoxide has been investigated by microwave spectroscopy, which has yielded rotational constants as well as information regarding its torsional potential for internal motion of the OH and CH_3 groups.[4] Hsieh and co-workers have studied the room-temperature vibrational spectra of the second through fifth OH-stretching overtones using photoacoustic spectroscopy and later extended their measurements of the third and fourth OH-stretching overtone regions using action spectroscopy in conjunction with laser-induced fluorescence (LIF) detection.[5,6] Using a complementary approach, we have probed the OH-stretching overtones of CH_3OOH using vibrational state-selected photodissociation both in a series of bulb measurements as well as, in a more limited manner, using free-jet expansion.[7] The excitation scheme that we used to investigate the bound OH-stretching overtone states is illustrated in Figure 1. The low-resolution overtone action spectra obtained in our previous study were interpreted rather successfully using an ab initio two-dimensional vibration−torsion model based on the adiabatic separation of the OH stretch and COOH torsion vibrational degrees of freedom in conjunction with a 2-D dipole moment surface.[7] The current study extends the results of our earlier work by focusing on the rotational band contours associated with spectra in the region of the two lowest OH-stretching overtones.

To facilitate discussion of the issues relevant for the present work, the adiabatic torsional potentials for the ground ($V_{OH} = 0$) and the first two OH-stretching overtone states ($V_{OH} = 2, 3$) obtained from our earlier work are shown in Figure 2, and the 2-D dipole moment surface $\boldsymbol{\mu}(r,\tau)$ involving the OH stretch (r) and COOH torsion (τ) coordinates is reproduced in Figure 3. As Figure 2 shows, due to the symmetry of the COOH adiabatic torsion potentials about $\tau = 180°$, the vibrational levels associated with these potentials occur in pairs. One wave function in the pair is symmetric with respect to reflection about a plane through the trans barrier at $\tau = 180°$ while the other is antisymmetric with respect to this plane. In Figure 2, we use + and − superscripts to denote these symmetries. We note that additional small splittings due to tunneling through the cis barrier as well those due to methyl torsion motion (A/E states) are also expected for each of the above vibrational levels.[4] However, these splittings are anticipated to be very small relative to our laser resolution (~ 0.08 cm^{-1}) and hence are neglected in the present analysis.

Our previous study highlighted the breakdown of the simple Franck−Condon model in simulating the OH-stretching overtone spectra of CH_3OOH when the 2-D dipole moment function $\boldsymbol{\mu}(r,\tau)$ is assumed to be separable, as is often done when invoking the bond dipole approximation.[6−10] In particular, we showed that properly accounting for the dependence of the dipole moment function on the COOH torsion gives rise to an antisymmetric component of the transition dipole moment, which, in turn, provides significant intensity to transitions associated with OH-stretching overtones that connect initial and final COOH torsional states having different reflection symmetry about the trans barrier (i.e., the $(+) \leftrightarrow (-)$ transitions shown by dashed arrows in Figure 2).[7] These transitions are not allowed when $\boldsymbol{\mu}(r,\tau)$ is assumed to be separable and expressed as $\boldsymbol{\mu}(r,\tau) = \boldsymbol{\mu}(r) + \boldsymbol{\mu}(\tau)$.[7] Furthermore, our previous results suggest that the fractional contribution of these $(+) \leftrightarrow (-)$ transitions are

---

[†] Part of the “Robert W. Field Festschrift”.

* To whom correspondence should be addressed. E-mail: asinha@ucsd.edu.

10.1021/jp902146z CCC: $40.75

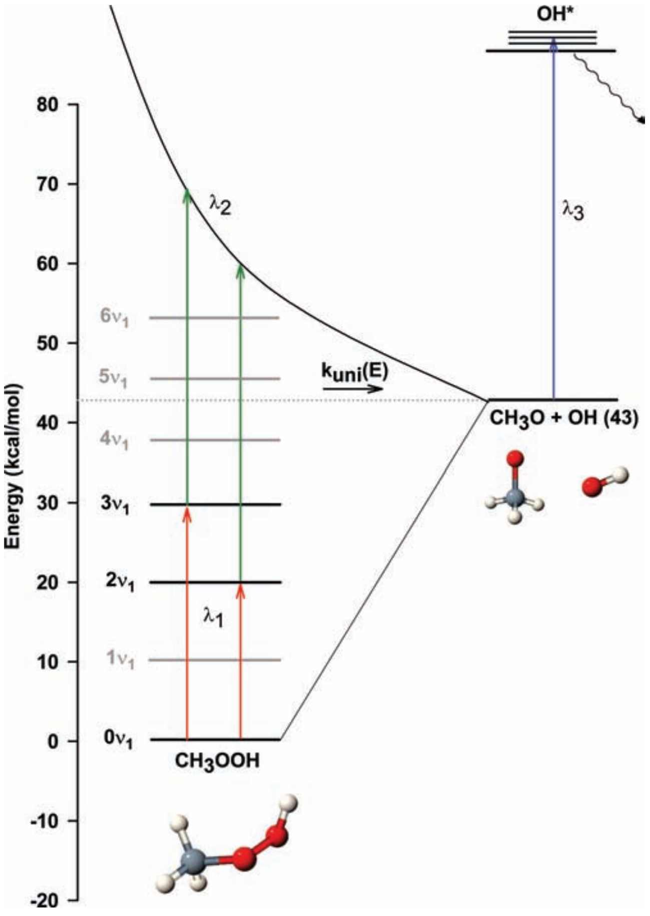

Figure 1. Schematic diagram of the state-selected photodissociation scheme used to record action spectra of the bound vibrational levels of methyl hydroperoxide. Infrared light at λ_1 excites the molecule to the target vibrational state from which they are then photodissociated using 532 nm light (λ_2). The OH fragments resulting from the state-selected photodissociation are probed by laser-induced fluorescence using λ_3.

the largest for the vibrational bands associated with the lowest-order OH-stretching overtones. In addition, we found that due to the combined symmetry of the torsional wave functions and the dipole moment components, shown, respectively, in Figures 2 and 3, the OH-stretching overtone bands of CH_3OOH connecting torsional states of different symmetry (i.e., (+) ↔ (−) transitions) involve the out-of-plane $\boldsymbol{\mu}_c$ component of the transition dipole moment, while transitions between torsion states of the same symmetry (i.e., (+) ↔ (+) and (−) ↔ (−)) involve the in-plane $\boldsymbol{\mu}_a$ and $\boldsymbol{\mu}_b$ component(s). As a consequence of this constraint, the rotational band types associated with these two classes of vibrational excitation, which are both present in each OH-stretching overtone band, are expected to be different, with their relative weights changing as the order of the overtone transition is changed.[7] These theoretical predictions motivated us to investigate the lowest OH-stretching overtone bands of CH_3OOH in greater detail, and the present study is directed toward examining the rotational band contours associated with the first and second OH-stretching overtones ($2\nu_{OH}$ and $3\nu_{OH}$) and their corresponding COOH torsional combination bands ($2\nu_{OH} + \nu_{COOH}$ and $3\nu_{OH} + \nu_{COOH}$) under jet-cooled conditions.

As we show below, an analysis of the band contours enables us to determine the vibrational band origins, effective rotational constants, as well as orientation of the transition moment(s) for the probed vibrational eigenstates. Our measurements also provide some insights into the intramolecular vibrational energy redistribution (IVR) associated with the zeroth-order OH-stretching overtone state and combination bands as revealed through the measured rotational line widths and band intensity anomalies. In addition, comparing the rotational contours of CH_3OOH with its deuterated analogue CD_3OOH (MHP-d_3) in the region of the $2\nu_{OH}$ and $2\nu_{OH} + \nu_{COOH}$ bands enables us to probe the role played by the vibrational modes of the methyl rotor in promoting IVR.

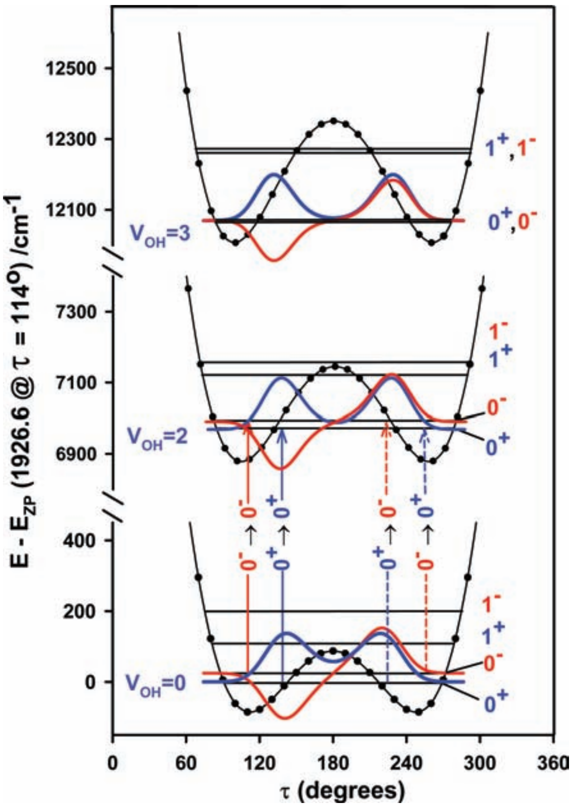

Figure 2. Adiabatic potentials for the COOH torsion coordinate associated with $V_{OH} = 0$, 2, and 3. Each torsional level occurs in pairs, with one state being symmetric about a plane through $\tau = 180°$ while the other is antisymmetric. These are respectively denoted using the + and − superscript labels in the figure. Transitions between initial and final torsional states of same symmetry and different symmetry are indicated, respectively, by the solid and dashed arrows. Also note that the torsion potential barrier heights increase with increasing OH-stretching excitation.

II. Experimental Approach

Room-temperature bulb experiments for recording overview spectra of methyl hydroperoxide were carried out in a manner similar to that described in our earlier work.[7,11] In order to minimize the influence of selective fragment probing on the recorded action spectrum in the bulb experiments, the OH fragment distributions were rotationally relaxed by adding N_2 buffer gas (~0.7 Torr) to the cell and increasing the time delay between the photolysis (λ_2) and probe laser (λ_3) to 1400 ns while keeping the delay between the IR vibrational excitation laser (λ_1) and the 532 nm photolysis laser (λ_2) fixed at 15 ns. The setup for conducting the jet-cooled experiments, which is the main focus of the present study, has also been described previously.[7] Briefly, the vacuum chamber consists of a cubic stainless steel cell with baffled side arms to introduce laser light, a side viewing port to collect fluorescence, and an additional port on top to hold the pulsed valve (General Valve, Series 9). The chamber is evacuated using a 6 in. diffusion pump (Varian:

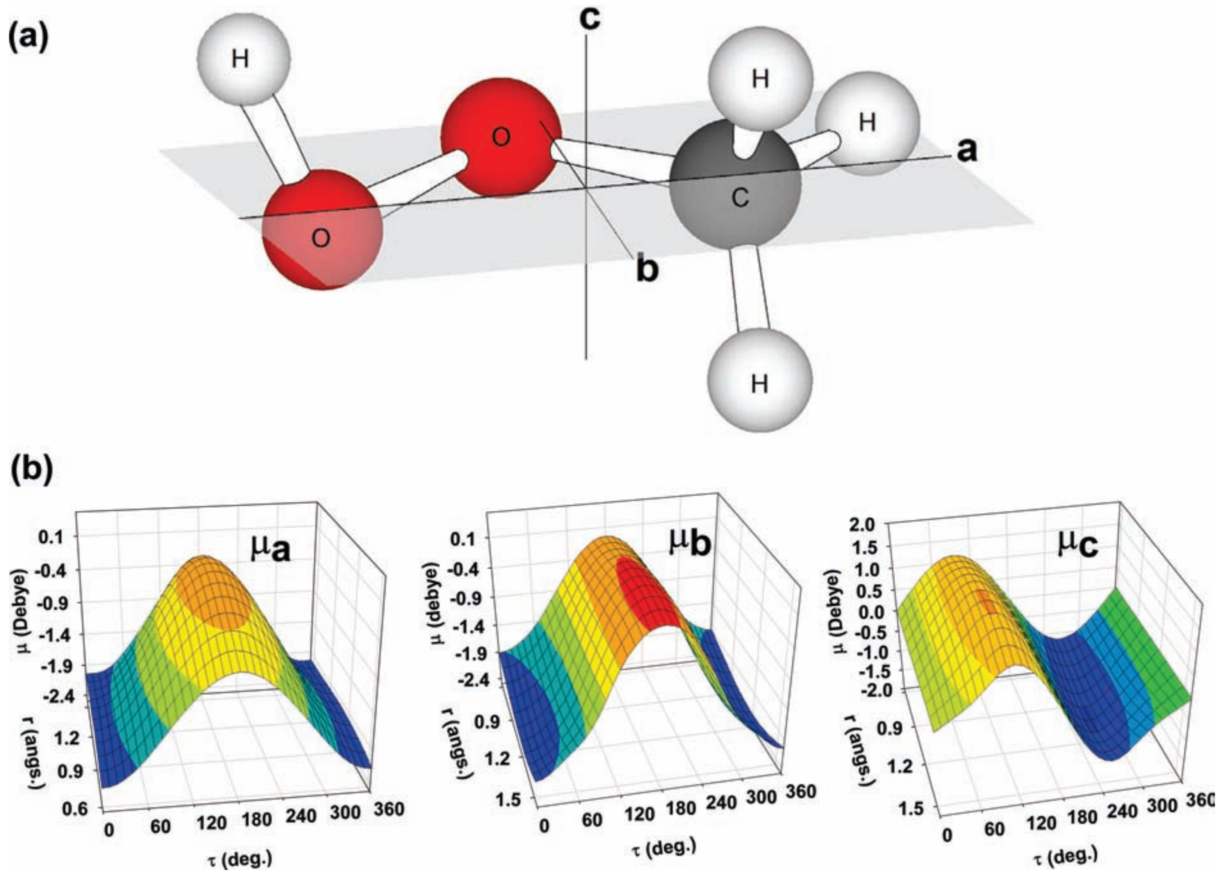

Figure 3. (a) Relative orientation of the molecular frame inertial axes in CH_3OOH. (b) Variation of the molecular frame components of the 2-D dipole moment function $\boldsymbol{\mu}(r,\tau)$ along the OH stretch and COOH torsion coordinates.

VHS-6), which is backed by a mechanical pump (Edwards: E2M30) through a liquid nitrogen cold trap. An aluminum gate valve separates the diffusion pump and chamber. A mixture of helium and methyl hydroperoxide is prepared by passing helium over a liquid methyl hydroperoxide sample maintained at 280 K. The helium carrier gas pressure is varied between 500 and 2280 Torr, depending on the extent of cooling desired. The gas mixture is then flowed into the pulsed valve, which operates at 20 Hz and has a 0.4 mm diameter orifice. For some measurements, the orifice diameter is increased to 1.0 mm. Typically, the valve exit is positioned 10 mm from the laser interaction region. In order to minimize sample loss, the valve is internally coated with halocarbon wax and fitted with a Teflon-coated spring and plunger, as well as a Kel-F poppet. A commercial pulsed valve driver (General Valve: Iota One) controls the valve open time and synchronization via an external trigger pulse. Typically, the valve is triggered ~800 μs prior to the laser firing and remains open for ~500 μs.

For survey scans, tunable infrared radiation (λ_1) in the vicinity of the first and second OH-stretching overtone is generated by an optical parametric oscillator (OPO: Spectra Physics MOPO-730), pumped by the third harmonic of a seeded Nd:YAG laser (Spectra Physics GCR-270). Typical idler pulse energies at the entrance to the chamber range between 4−6 mJ in the region of the first OH-stretching overtone ($2\nu_{OH}$) and 10−12 mJ for the second OH-stretching overtone ($3\nu_{OH}$). The MOPO laser has a line width of ~0.4 cm^{-1}. The doubled 532 nm output of a second Nd: YAG laser (Continuum: NY81−20) is split, and a portion of this light is used to further excite the vibrationally state-selected molecules to a dissociative electronic excited state (i.e., $\lambda_2 = 532$ nm; see Figure 1). The λ_2 beam, with pulse energies of ~65 mJ, counterpropagates relative to the IR beam and is gently focused inside of the vacuum chamber using a 500 mm lens with its focal point shifted by 2 in. from the interaction region. A delay generator (BNC: Series 555) synchronizes the firing of the IR excitation and photolysis lasers, with their delay set at ~15 ns. The OH product is probed (λ_3) via the A−X (1,0) transition using the doubled output of a second dye laser (Continuum: ND60) operating with R590 dye and pumped by the residual 532 nm output of the Nd:YAG laser that provides the λ_2 beam. The 282 nm probe light has a bandwidth of ~0.13 cm^{-1} and is greatly attenuated to prevent direct photolysis of the CH_3OOH sample. The probe laser beam is temporally delayed by 10 ns relative to the photolysis laser ($\lambda_2 = 532$ nm) using an optical delay line and co-propagates along the same direction. The OH fluorescence is collected using an f/1 lens system and imaged onto an end-on photomultiplier tube (PMT, EMI 9813QB). A color glass filter (Schott UG-11, 2 mm) and a set of 266 nm dichroics, respectively, provide rejection of the 532 (λ_2) and 282 nm (λ_3) scattered light while allowing collection of the OH A−X (1,0) fluorescence. The signal from the PMT is amplified (×5) using a preamp (SRS: SR445A) and then sent to a gated integrator (LeCroy, 2249SG ADC) and finally to a computer for storage.

For the high-resolution scans of the $2\nu_{OH}$ and $2\nu_{OH} + \nu_{COOH}$ bands, we use difference frequency mixing (DFM) to generate the IR radiation. In these experiments, the output of a dye laser (Continuum: ND60) operating with a R610 + R640 dye mixture is combined with the seeded fundamental of a Nd:YAG laser (Continuum: NY82-20) in a $LiNbO_3$ crystal to generate the IR light. Typical dye laser and Nd:YAG fundamental input energies for DFM range between 22−25 and 30−35 mJ, respectively. The resulting IR output power is between 1.5 and 2.5 mJ with a bandwidth of 0.08 cm^{-1} (fwhm). In order to ensure spectral

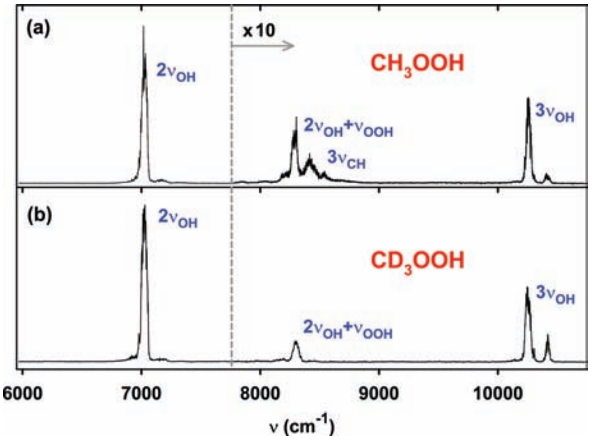

Figure 4. (a) Room-temperature survey spectrum of CH_3OOH over the $2\nu_{OH}$−$3\nu_{OH}$ region under bulb condition. (b) Room-temperature survey spectrum of CD_3OOH over the $2\nu_{OH}$−$3\nu_{OH}$ region also under bulb condition. Note that the broad features in the vicinity of ~8400 cm^{-1} are absent in this spectrum.

calibration and monitoring of the laser line width, a portion of the IR beam is directed into a photoacoustic cell containing water vapor, and its spectrum is simultaneously recorded and compared against the HITRAN database.[12] The synthesis of methyl hydroperoxide has been described in our previous work and basically follows the procedure reported by Vaghjiani and Ravishankara.[7,13] The synthesis of CD_3OOH follows an analogous scheme with dimethyl sulfate being replaced by its deuterated analogue.

III. Results and Discussion

A. Medium-Resolution Survey Spectrum of CH_3OOH and CD_3OOH. A room-temperature overview spectrum of methyl hydroperoxide covering the $2\nu_{OH}$−$3\nu_{OH}$ spectral region is shown in Figure 4a. This action spectrum is obtained by scanning the MOPO laser from 6500 to 11 000 cm^{-1} while monitoring OH fragments in the $N = 2$ rotational state. The prominent bands appearing in Figure 4a at ~7000 and ~10 260 cm^{-1} correspond, respectively, to the first and second OH-stretching overtones ($2\nu_{OH}$ and $3\nu_{OH}$) of CH_3OOH. The weak feature at ~10 420 cm^{-1} is assigned to a OH stretch/COOH torsion combination band built on the second OH-stretching overtone (i.e., $3\nu_{OH} + \nu_{COOH}$). A glance at Figure 4a also shows additional spectral features located midway between the $2\nu_{OH}$ and the $3\nu_{OH}$ bands. We assign the sharp feature at ~8290 cm^{-1} to the OH stretch/HOO bend combination band ($2\nu_{OH} + \nu_{OOH}$) and the series of broad peaks to the red and blue of this at 8203, 8417, 8538, and 8676 cm^{-1} to bands involving the second overtone of the CH stretch ($3\nu_{CH}$). This assignment, though tentative, is supported by comparing with the spectrum of the CD_3OOH isotopomer shown in Figure 4b, taken under similar conditions. Upon deuteration at the methyl site, we find that the spectral feature near ~8290 cm^{-1} appears cleaner, dominated by a single sharp band without the presence of the broad diffuse features that appear in the corresponding CH_3OOH spectrum over the same region. Furthermore, on the basis of the results shown in Table 1, which lists the frequencies, anharmonic couplings, and MHP-d_3 isotope shifts calculated at the MP2/aug-cc-pVTZ level of theory, we see that the $2\nu_{OH} + \nu_{OOH}$ stretch−bend combination mode (i.e., $2\nu_1 + \nu_8$) is not expected to shift substantially (~4 cm^{-1}) upon deuterium substitution at the methyl site. By contrast, the C−D-stretching modes are expected to shift by about 800 cm^{-1} per quanta of excitation relative to the C−H stretch. Experimentally, upon deuterium substitution, we find a small shift of ~8 cm^{-1} for the sharp feature at ~8300 cm^{-1}, consistent with it being assigned as the $2\nu_1 + \nu_8$ band. The $3\nu_{CD}$ stretching modes, by contrast, are expected to shift by ~2500 cm^{-1} relative to their C−H-stretching counterpart and thus fall in the region around 6000 cm^{-1}, consistent with their absence in Figure 4b.

In order to extract additional information regarding the vibrational bands appearing in Figure 4, we next turn our attention to the medium-resolution jet-cooled survey spectra. We anticipate that cooling the molecule will potentially reveal features hidden by spectral congestion at room temperature. Jet-cooled spectra of the $2\nu_{OH}$, $3\nu_{CH}$, $2\nu_{OH} + \nu_{OOH}$, and $3\nu_{OH}$ regions recorded using the MOPO laser are shown in Figure 5a−c along with their room-temperature counterparts. In each panel of Figure 5, the effect of reducing the rotational temperature on the action spectra is readily evident. Aside from the bands appearing narrower and more resolved upon cooling, we notice that the band origins of several of the bands shift away from their apparent value at room temperature. Interestingly, in the region of the $2\nu_{OH}$ band, the jet-cooled spectrum reveals an additional feature at 7150 cm^{-1}, which is barely discernible in the room-temperature spectrum (see Figure 5a). On the basis of our 2-D model,[7] we assign this band to the OH stretch/COOH torsion combination band $2\nu_{OH} + \nu_{COOH}$. It is also worth noting that while we observe significant narrowing of the band profiles involving the OH modes (stretch, bend, and torsion), the profiles of the CH-stretching modes ($3\nu_{CH}$) remain significantly broadened even under free-jet expansion conditions. The CH bands span a region of ~500 cm^{-1} in the spectrum of Figure 5b, and the extensive broadening suggests that these modes are strongly coupled to a large number of "dark" vibrational bath states.

TABLE 1: Harmonic Frequencies, Anharmonicities, and Isotope Shifts of CH_3OOH Computed at MP2/aug-cc-pVTZ (cm^{-1})

$(\omega_e)_i$	3777	3179	3151	3061	1532	1490	1464	1359	1211	1181	1060	870	447	261	171
d_3 shift	0	820	812	870	454	391	109	3.5	111	150	78.7	55.0	41.6	59.5	1.9
$(\omega_e\chi_e)_{ij}$	1	2	3	4	5	6	7	8	9	10	11	12	13	14	15
1	−84.4														
2	−0.84	−36.7													
3	−0.71	−28.8	−31.4												
4	−0.82	−53.4	−87.2	−19.0											
5	−0.43	−3.84	−17.5	−20.5	−3.58										
6	−0.02	−17.8	−10.4	−0.42	−5.28	−8.75									
7	−0.28	−13.4	−7.30	19.9	−4.63	−6.43	−10.6								
8	−27.6	−0.73	0.74	0.06	−0.83	−0.80	−1.37	−9.89							
9	0.11	−5.05	−3.40	−3.03	−3.95	−5.13	−8.33	−29.5	−2.63						
10	−0.56	−3.04	−3.06	−3.98	−10.7	−6.67	−3.07	−1.48	−0.08	−1.82					
11	−2.78	−1.16	3.78	1.17	−2.13	−2.69	−6.17	−5.86	−10.4	−7.98	−6.91				
12	−3.06	−1.26	0.32	−0.13	−0.79	−0.99	−1.19	−11.4	−2.53	−0.67	−6.71	−4.56			
13	0.27	−0.66	0.43	0.17	0.42	−1.04	−0.26	−1.15	−1.55	0.55	−4.99	−4.56	0.38		
14	0.24	−0.68	2.14	1.23	−1.71	1.16	2.10	−0.06	−3.52	−1.62	0.43	−1.33	2.14	−6.16	
15	9.13	2.83	−2.84	0.09	1.71	−1.40	−0.13	−8.83	14.0	1.04	8.98	0.11	−2.30	−5.39	−50.4

B. Higher-Resolution Cold Spectrum of CH_3OOH $2\nu_{OH}$ and $2\nu_{OH} + \nu_{COOH}$ Bands. The survey spectra presented in the previous section were recorded using the MOPO laser. In order to extract further details, we have also recorded spectra of the $2\nu_{OH}$ and $2\nu_{OH} + \nu_{COOH}$ bands under higher resolution (~0.08 cm^{-1}) and colder temperatures. In these experiments, we use difference frequency mixing to generate the IR light (λ_1) and achieve greater cooling by increasing the helium carrier gas backing pressure to ~3 atm. Action spectra of the $2\nu_{OH}$ and $2\nu_{OH} + \nu_{COOH}$ bands taken under these conditions are shown in Figure 6a and b, respectively. As can be seen from the figures, increased resolution and cooling leads to a more structured spectrum for both bands, with their rotational contours now becoming discernible. Simulation of the resulting rotational band contours is simplified by recognizing that at the temperature of these experiments, only one initially populated vibrational level contributes significantly to the observed band intensity. As shown in Figure 2, the $V_{OH} = 0$ ground vibrational level of CH_3OOH is split into two torsional levels labeled as $|0\ 0^+\rangle$ and $|0\ 0^-\rangle$. Here, we use the notation $|V_{OH}\ V_\tau^{+/-}\rangle$ to specify a vibration−torsion state, with the first and second numbers inside of the bracket specifying, respectively, the number of quanta in the OH stretch and COOH torsion coordinates and the +/− superscript giving the torsional state symmetry. According to microwave data, the $|0\ 0^-\rangle$ level lies 14.97 cm^{-1} above the $|0\ 0^+\rangle$ level.[4] Our jet expansion corresponds to a rotational temperature of ~5 K. Thus, if we assume that the low-frequency torsional vibrations are characterized by a similar temperature, the population in the $|0\ 0^-\rangle$ level is expected to be less than ~1% of the total population. Hence, all transitions originating from the $|0\ 0^-\rangle$ level can be neglected, and we focus on transitions originating from only the $|0\ 0^+\rangle$ state. With this basic fact in mind, we first discuss the fitting of the $2\nu_{OH}$ band contour before presenting results for the $2\nu_{OH} + \nu_{COOH}$ combination band.

On the basis of our 2-D ab initio model, both the $|0\ 0^+\rangle \rightarrow |2\ 0^+\rangle$ and $|0\ 0^+\rangle \rightarrow |2\ 0^-\rangle$ vibrational transitions contribute to the $2\nu_{OH}$ band intensity. We estimate the relative contribution expected for each by evaluating the following transition moment matrix elements

$$\boldsymbol{\mu}_\alpha = \langle 2\ 0^+ | \boldsymbol{\mu}_\alpha(r,\tau) | 0\ 0^+ \rangle \qquad \alpha = \mathbf{a}, \mathbf{b}, \text{ or } \mathbf{c} \tag{1}$$

and

$$\boldsymbol{\mu}_\alpha = \langle 2\ 0^- | \boldsymbol{\mu}_\alpha(r,\tau) | 0\ 0^+ \rangle \qquad \alpha = \mathbf{a}, \mathbf{b}, \text{ or } \mathbf{c} \tag{2}$$

In the above equations, $\boldsymbol{\mu}_\alpha(r,\tau)$ are the components of the 2-D molecular frame dipole moment function obtained from ab initio calculation, while the initial and final state wave functions are product functions involving the adiabatically separated OH stretch and COOH torsion coordinates, generated by the 2-D model.[7] The oscillator strength of a transition is proportional to the square of the above transition moment matrix elements (i.e., $|\boldsymbol{\mu}_\mathbf{a}|^2$, $|\boldsymbol{\mu}_\mathbf{b}|^2$, and $|\boldsymbol{\mu}_\mathbf{c}|^2$), and these are given in Table 2 for the transitions of interest. The calculations reveal that the $|0\ 0^+\rangle \rightarrow |2\ 0^+\rangle$ transition arises solely from the $\boldsymbol{\mu}_\mathbf{a}$ component, while the $|0\ 0^+\rangle \rightarrow |2\ 0^-\rangle$ transition involves only $\boldsymbol{\mu}_\mathbf{c}$. We note from the first row in Table 2 that the $\boldsymbol{\mu}_\mathbf{b}$ component contributes little to either the $|0\ 0^+\rangle \rightarrow |2\ 0^+\rangle$ or the $|0\ 0^+\rangle \rightarrow |2\ 0^-\rangle$ transitions. The calculations also predict the separation between the $|2\ 0^+\rangle$ and $|2\ 0^-\rangle$ final states to be ~1.2 cm^{-1}. Hence, the results of the 2-D ab initio model suggest that the $2\nu_{OH}$ band is made up of two nearly overlapping vibrational excitations, with one involving an "a-"type rotational band contour associated with the $|0\ 0^+\rangle \rightarrow |2\ 0^+\rangle$ excitation while the other is a "c-"type contour arising from the $|0\ 0^+\rangle \rightarrow |2\ 0^-\rangle$ component. Furthermore, the results given in Table 2 suggest that the ratio of the a-type to c-type contribution is expected to be ~69%.

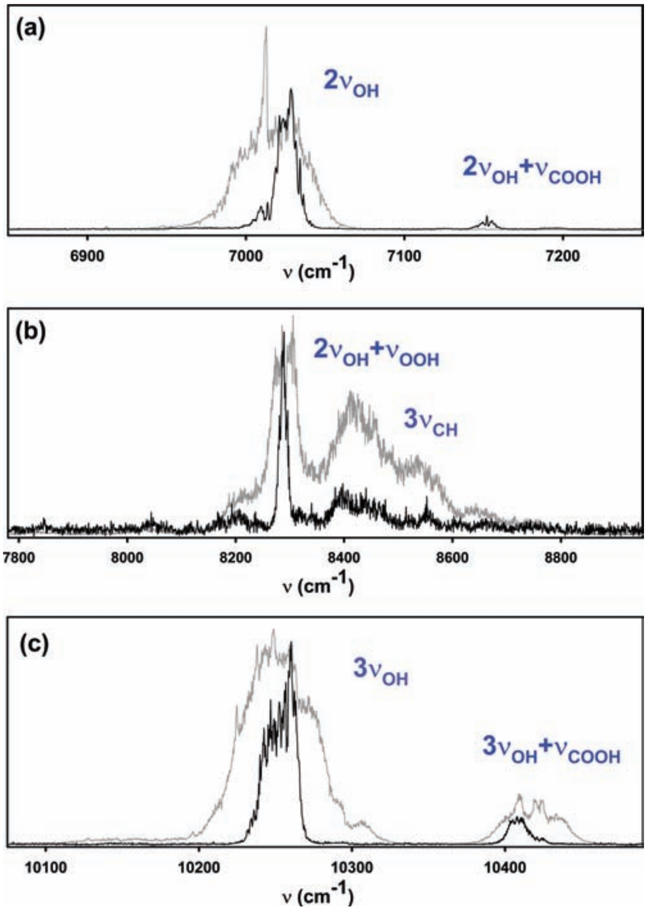

Figure 5. Comparison of room-temperature (in gray) versus jet-cooled spectra of CH_3OOH over the regions of (a) $2\nu_{OH}$ and $2\nu_{OH} + \nu_{COOH}$ bands, (b) $2\nu_{OH} + \nu_{HOO}$ and $3\nu_{CH}$ bands, and (c) $3\nu_{OH}$ and $3\nu_{OH} + \nu_{COOH}$ bands. All spectra are recorded using the MOPO with ~0.4 cm^{-1} resolution and for the jet-spectra using modest expansion conditions (500 Torr of He).

Aside from needing to know the transition moment(s), the associated rotational constants are also required for the simulations. The rotational parameters for the starting $|0\ 0^+\rangle$ level are known from microwave data and are summarized in Table 3; hence, only those for the final $|2\ 0^{+/-}\rangle$ states are needed. We started our simulations by selecting the upper-state rotational constants to be identical to those of the ground state and then systematically allowed them to vary until optimum fits were obtained. We used the PGOPHER rotational simulation program to fit the spectrum treating the molecule as an asymmetric top (*A*-reduction, *I*^{r}-representation) having C_1 point group symmetry.[14] Our best fit for the $2\nu_{OH}$ band is given by the dashed line shown in Figure 6a. This optimized rotational band contour is obtained by running the simulation while varying the relative weights of the transition moments, upper-state rotational constants, the beam rotational temperature, and line widths of the rotational transitions. The simulation confirms that indeed, two vibration−torsion transitions ($|0\ 0^+\rangle \rightarrow |2\ 0^+\rangle$ and $|0\ 0^+\rangle \rightarrow |2\ 0^-\rangle$) are involved in making up the $2\nu_{OH}$ spectrum. The $|0\ 0^+\rangle \rightarrow |2\ 0^+\rangle$ excitation has its band origin at $\nu_0 = 7024.65$

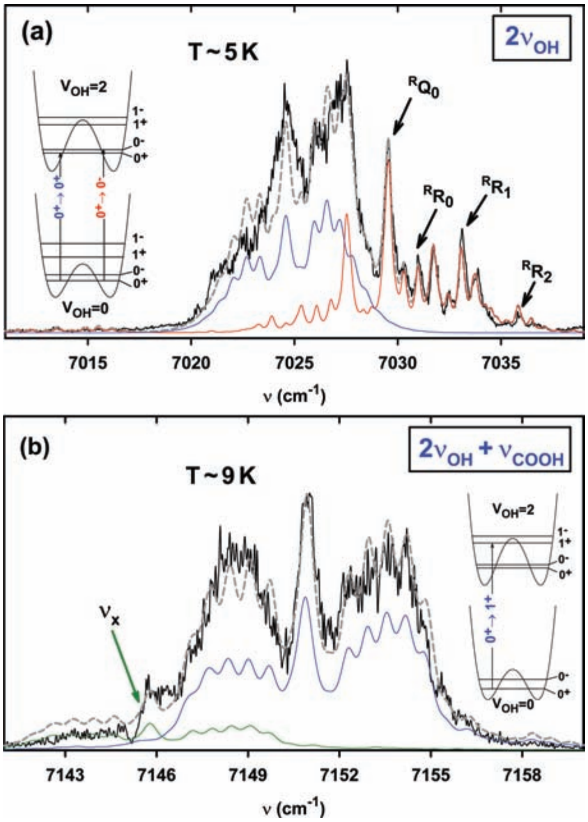

Figure 6. (a) Jet-cooled spectra of the $2\nu_{\mathrm{OH}}$ band of CH_3OOH recorded at $\sim$0.08 cm^{-1} resolution and 5 K obtained by probing the OH ($^2\Pi_{3/2}$, $v = 0$) fragments in the $N = 5$ rotational state. On the basis of our 2-D ab initio model, the band is composed of two excitations involving the $|0\ 0^{+}\rangle \rightarrow |2\ 0^{+}\rangle$ and the $|0\ 0^{+}\rangle \rightarrow |2\ 0^{-}\rangle$ excitations. The $|0\ 0^{+}\rangle \rightarrow |2\ 0^{+}\rangle$ excitation is of pure a-type, while $|0\ 0^{+}\rangle \rightarrow |2\ 0^{-}\rangle$ is pure c-type. The overall simulation, represented by the dashed line, exhibits differences primarily in the vicinity of 7025 cm^{-1} due to the presence of a dark state. (b) Jet-cooled spectra of the $2\nu_{\mathrm{OH}} + \nu_{\mathrm{COOH}}$ combination band of CH_3OOH recorded at $\sim$0.08 cm^{-1} resolution and 9 K. On the basis of our 2-D ab initio model, the band is composed of a single excitation involving the $|0\ 0^{+}\rangle \rightarrow |2\ 1^{+}\rangle$ transition. The overall simulation, represented by the dashed line, also includes the dark state located at around 7146 cm^{-1}.

cm^{-1} and is purely a-type, while the $|0\ 0^{+}\rangle \rightarrow |2\ 0^{-}\rangle$ component with origin at $\nu_0 = 7028.55$ cm^{-1} is a pure c-type band. The individual contours for the $|0\ 0^{+}\rangle \rightarrow |2\ 0^{+}\rangle$ and the $|0\ 0^{+}\rangle \rightarrow |2\ 0^{-}\rangle$ transitions making up the $2\nu_{\mathrm{OH}}$ band are represented by the solid colored lines in Figure 6a. The P-, Q-, and R- branches in the figure are labeled according to their prolate symmetric top limit ($^{\Delta K_a}\Delta J_{K''_a}$). For example, the peak labeled $^{R}Q_0$ contain several transitions involving $\Delta J = 0$ with $K''_a = 0$ and $K'_a = 1$. The analysis show that the intensity of the symmetry changing $|0\ 0^{+}\rangle \rightarrow |2\ 0^{-}\rangle$ excitation is significant, corresponding to $\sim$70% of that for the $|0\ 0^{+}\rangle \rightarrow |2\ 0^{+}\rangle$ excitation, which connects initial and final states of the same torsional symmetry. A single excitation involving only transitions between initial and final states of the same torsional symmetry, as would be expected from using the simple bond dipole approximation, is unable to explain the spectrum.[5−7] We note that deviations from the bond dipole approximation have been observed in other systems as well.[15,16]

In our simulations of the $2\nu_{\mathrm{OH}}$ band, we observe perceptible deviation of the fits in the vicinity of 7025 cm^{-1}, near the band origin of the $|0\ 0^{+}\rangle \rightarrow |2\ 0^{+}\rangle$ transition, hinting at the presence of an unidentified "dark" satellite state there. Moreover, we find significant differences in the individual rotational line widths associated with the two vibrational transitions with the rotational levels of the $|2\ 0^{+}\rangle$ state being broadened, on average, by 0.70 cm^{-1} (fwhm) while those of the $|2\ 0^{-}\rangle$ state have a width of 0.25 cm^{-1}. From the fits, we obtain approximate effective rotational constants for the $|2\ 0^{+}\rangle$ and $|2\ 0^{-}\rangle$ levels given in the left portion of Table 4. The uncertainty in these effective rotational constants is estimated to be $\sim$2−3%. The present data do not allow us to detect differences in the rotational constants for the two upper states, and we find that the fits are more sensitive to the rotational parameters of the $|2\ 0^{-}\rangle$ level, whose intensity profile contributes primarily to the blue side of the $2\nu_{\mathrm{OH}}$ band, away from the perturbing dark state at $\sim$7025 cm^{-1}. Our study also provides the first measurements of the torsional splitting between the 0^{+} and 0^{-} levels associated with the $2\nu_{\mathrm{OH}}$ overtone state. The difference in band origin between the $|0\ 0^{+}\rangle \rightarrow |2\ 0^{+}\rangle$ and $|0\ 0^{+}\rangle \rightarrow |2\ 0^{-}\rangle$ transitions making up the $2\nu_{\mathrm{OH}}$ band ($\nu_0 = 7024.65$ and 7028.55 cm^{-1}, respectively) implies that this separation is $\sim$3.9 cm^{-1}. This splitting is in reasonable accord with the results of ab initio calculation, which predicts a value of 1.2 cm^{-1}.[7] The decrease in the 0^{+} and 0^{-} level separation in going from $V_{\mathrm{OH}} = 0$, where it is 14.97 cm^{-1},[4] to its value at $V_{\mathrm{OH}} = 2$ reflects the increase in the COOH torsional potential barrier height with increasing OH-stretching excitation in CH_3OOH (see Figure 2).[5−7,17−19]

We next discuss the fit for the $2\nu_{\mathrm{OH}} + \nu_{\mathrm{COOH}}$ combination band which occurs $\sim$125 cm^{-1} to the blue of the $2\nu_{\mathrm{OH}}$ band and is shown in Figure 6b. Our 2-D ab initio model suggests that at 9 K, this combination band has contribution from primarily the $|0\ 0^{+}\rangle \rightarrow |2\ 1^{+}\rangle$ transition. The other transition potentially associated with this band is the $|0\ 0^{+}\rangle \rightarrow |2\ 1^{-}\rangle$ excitation. This transition, however, is fairly weak and occurs at $\sim$7383 cm^{-1}, outside of our present spectral region of interest. On the basis of the ab initio results, the $|0\ 0^{+}\rangle \rightarrow |2\ 1^{+}\rangle$ transition is expected to be a hybrid band involving both the $\boldsymbol{\mu}_{\mathbf{a}}$ and $\boldsymbol{\mu}_{\mathbf{b}}$ components of the transition moment in a ratio of 1.0:0.62; contribution from the $\boldsymbol{\mu}_{\mathbf{c}}$ component is predicted to be negligible. In order to fit the combination band contour, we used an average rotational line width of 0.5 cm^{-1} (fwhm). Further, for the simulation to reproduce the experiments, we also found it necessary to include contribution from a "dark" satellite state at $\nu_0 = 7145.9$ cm^{-1} (labeled υ_x in Figure 6b), which carries $\sim$20% the intensity of the main $|0\ 0^{+}\rangle \rightarrow |2\ 1^{+}\rangle$ transition. The best fit for the $2\nu_{\mathrm{OH}} + \nu_{\mathrm{COOH}}$ combination band, represented by the dashed line in Figure 6b, is therefore a sum of contribution from both of these bands. It is important to note that this dark-state transition is unaccounted for by our simple 2-D model, which only considers transitions involving the OH stretch and COOH torsion. We also point out that the dark-state feature is definitely not due to a hot-band transition as we find that changing the jet temperature does not affect its relative band intensity. The final parameters extracted for the $2\nu_{\mathrm{OH}} + \nu_{\mathrm{COOH}}$ band analysis are summarized in left portion of Table 5. Within our resolution, the upper-state rotational constants for the $|2\ 1^{+}\rangle$ torsion state are found to be identical to those of the pure stretching states $|2\ 0^{+/-}\rangle$, although the orientations of their respective transition moment are different. The fact that $|2\ 1^{+}\rangle$ and $|2\ 0^{+/-}\rangle$ have similar rotational constant is consistent with microwave data for the $V_{\mathrm{OH}} = 0$ ground state, where the $|0\ 0^{+}\rangle$ and $|0\ 1^{+}\rangle$ states are found to have A and C rotational constants that differ by less than 0.07% and B rotational constant that differ by less than 0.23%.[4]

Finally, the measured orientation of the transition moments for the $2\nu_{\mathrm{OH}}$ and $2\nu_{\mathrm{OH}} + \nu_{\mathrm{COOH}}$ bands requires some discussion. For the $2\nu_{\mathrm{OH}}$ band, although it is clear from the dipole moment

TABLE 2: CCSD(T)/cc-pVTZ Transition Dipole Moments for the Various Matrix Elements $\langle 0\ 0^{+/-}|\boldsymbol{\mu}_{\alpha}|2\ 0^{+/-}\rangle$[a]

	$\langle 2\ 0^{+}|$				$\langle 2\ 0^{-}|$	
substates	$|\boldsymbol{\mu}_{a}|$	$|\boldsymbol{\mu}_{b}|$	$|\boldsymbol{\mu}_{c}|$	$|\boldsymbol{\mu}_{a}|$	$|\boldsymbol{\mu}_{b}|$	$|\boldsymbol{\mu}_{c}|$
$|0\ 0^{+}\rangle$	1.2×10^{-2} (1.0)	4.8×10^{-4} (0.04)	2.5×10^{-6} (~0)	3.1×10^{-6} (~0)	8.4×10^{-8} (~0)	1.0×10^{-2} (0.83)
$|0\ 0^{-}\rangle$	2.6×10^{-6} (~0)	4.8×10^{-8} (~0)	1.0×10^{-2} (0.83)	1.2×10^{-2} (1.0)	1.1×10^{-4} (0.01)	2.0×10^{-6} (~0)

[a] The values in parentheses are normalized with respect to the $\langle 2\ 0^{+}|\boldsymbol{\mu}_{a}|0\ 0^{+}\rangle$ transition.

TABLE 3: Spectroscopic Parameters for the Few Lowest Torsional States Associated with $V_{OH} = 0$ for both CH_3OOH and CD_3OOH (cm^{-1})

	$|0\ 0^{+}\rangle$		$|0\ 0^{-}\rangle$		$|0\ 1^{+}\rangle$		$|0\ 1^{-}\rangle$	
	expt.[a]	ab initio[b]	expt.[a]	ab initio[b]	expt.[a]	ab initio[b]	expt.[a]	ab initio[b]
				CH_3OOH				
A''	1.4286	1.4123	1.4239	1.4129	1.4289	1.4203	1.4222	1.4203
B''	0.3503	0.3501	0.3495	0.3501	0.3511	0.3527	0.3502	0.3527
C''	0.3020	0.3018	0.3027	0.3018	0.3018	0.3004	0.3026	0.3009
ν_0	0	0	14.97	8.4[c]	130[d]	124.8[c]	191[d]	197.4[c]
				CD_3OOH				
A''	1.1135[e]	1.1006	1.1135[e]	1.1006		1.1058		1.1058
B''	0.3004[e]	0.2992	0.3004[e]	0.2992		0.3010		0.3010
C''	0.2627[e]	0.2627	0.2627[e]	0.2627		0.2616		0.2616
ν_0	0	0	14.85[d]					

[a] From ref 4, except where noted otherwise. [b] From MP2/aug-cc-pVTZ, except where noted otherwise. [c] From the CCSD(T)/cc-pVTZ 2-D model. [d] This work. [e] The values from ref 4 are scaled using the ratio of rotational constants from the MP2/aug-cc-pVTZ level.

TABLE 4: Parameters Used to Simulate the Jet-Cooled Rotational Band Contours of the $2\nu_{OH}$ Band for CH_3OOH and CD_3OOH[a]

	CH_3OOH		CD_3OOH	
	$|0\ 0^{+}\rangle \rightarrow |2\ 0^{+}\rangle$	$|0\ 0^{+}\rangle \rightarrow |2\ 0^{-}\rangle$	$|0\ 0^{+}\rangle \rightarrow |2\ 0^{+}\rangle$	$|0\ 0^{+}\rangle \rightarrow |2\ 0^{-}\rangle$
ν_0	7024.65 ± 0.05	7028.55 ± 0.05	7024.93 ± 0.05	7028.47 ± 0.05
$\Delta\nu$ (fwhm)	0.7 ± 0.1	0.25 ± 0.1	0.65 ± 0.1	0.45 ± 0.1
A'	1.4067	1.4067	1.1077	1.1077
B'	0.3480	0.3480	0.3013	0.3013
C'	0.3030	0.3030	0.2610	0.2610
$\boldsymbol{\mu}_{a}$	1	0	1	0
$\boldsymbol{\mu}_{b}$	0	0	0	0
$\boldsymbol{\mu}_{c}$	0	1	0	1
I[b]	1	0.7	1	0.7

[a] In cm^{-1}. The transition moments are relative to the $\langle 2\ 0^{+}|\boldsymbol{\mu}_{a}|0\ 0^{+}\rangle$ transition. [b] Intensities are relative to the $|0\ 0^{+}\rangle \rightarrow |2\ 0^{+}\rangle$ transition.

TABLE 5: Parameters Used to Simulate the Jet-Cooled Rotational Band Contours of the $2\nu_{OH} + \nu_{COOH}$ Combination Band for CH_3OOH and CD_3OOH[a]

	CH_3OOH		CD_3OOH
	$|0\ 0^{+}\rangle \rightarrow |2\ 1^{+}\rangle$	$|0\ 0^{+}\rangle \rightarrow |\upsilon_{x}{}^{+}\rangle$	$|0\ 0^{+}\rangle \rightarrow |2\ 1^{+}\rangle$
ν_0	7151.04 ± 0.05	7145.90 ± 0.05	7149.68 ± 0.05
$\Delta\nu$ (fwhm)	0.5 ± 0.1	0.5 ± 0.1	0.21 ± 0.03
A'	1.4067	1.4067	1.1077
B'	0.3480	0.3480	0.3013
C'	0.3030	0.3030	0.2610
$\boldsymbol{\mu}_{a}$	1	1	1
$\boldsymbol{\mu}_{b}$	0.50	0.63	0.52
$\boldsymbol{\mu}_{c}$	0	0	0
I[b]	1	0.2	1

[a] In cm^{-1}. The transition moments are relative to the $\langle 2\ 1^{+}|\boldsymbol{\mu}_{a}|0\ 0^{+}\rangle$ transition. [b] Intensities are relative to the $|0\ 0^{+}\rangle \rightarrow |2\ 1^{+}\rangle$ transition.

TABLE 6: Parameters Used to Simulate the Jet-Cooled Rotational Band Contours of the $3\nu_{OH} + \nu_{COOH}$ Combination Band for CH_3OOH at 19 K[a]

	$|0\ 0^{+}\rangle \rightarrow |3\ 1^{+}\rangle$	$|0\ 0^{-}\rangle \rightarrow |3\ 1^{-}\rangle$	$|0\ 0^{+}\rangle \rightarrow |\upsilon_{y}{}^{+}\rangle$
ν_0	10 407.85 ± 0.1	10 420.65 ± 0.1	10 421.1 ± 0.1
$\Delta\nu$ (fwhm)	1.0 ± 0.15	1.0 ± 0.15	1.0 ± 0.15
A'	1.4140	1.4140	1.4140
B'	0.3562	0.3562	0.3562
C'	0.3062	0.3062	0.3062
$\boldsymbol{\mu}_{a}$	1	1	1
$\boldsymbol{\mu}_{b}$	0.23	0.26	0.23
$\boldsymbol{\mu}_{c}$	0	0	0
I[b]	1	0.33	0.25

[a] In cm^{-1}. The transition moments are relative to the $\langle 3\ 1^{+}|\boldsymbol{\mu}_{a}|0\ 0^{+}\rangle$ transition. [b] Intensities are relative to the $|0\ 0^{+}\rangle \rightarrow |3\ 1^{+}\rangle$ transition.

symmetry (Figure 3b) that the $|0\ 0^{+}\rangle \rightarrow |2\ 0^{-}\rangle$ transition must be of pure c-type, it is by no means obvious from the figure why the $|0\ 0^{+}\rangle \rightarrow |2\ 0^{+}\rangle$ transition does not have any contribution from $\boldsymbol{\mu}_{b}$. This is especially puzzling given that the $\boldsymbol{\mu}_{b}$ component of the dipole moment is large in CH_3OOH and appears to be of the right symmetry with respect to reflection about a plane through the barrier at $\tau = 180°$ (Figure 3b). To clarify this point, we have examined the 2-D transition dipole moment integrals for the $2\nu_{OH}$ band in terms of their separate contributions from both the OH and COOH coordinates. Figure 7a,b shows the results of integrating the 2-D transition moment matrix elements $\langle 0\ 0^{+}|\boldsymbol{\mu}_{a}(r,\tau)|\ 2\ 0^{+}\rangle$ and $\langle 0\ 0^{+}|\boldsymbol{\mu}_{b}(r,\tau)|\ 2\ 0^{+}\rangle$ first just over the

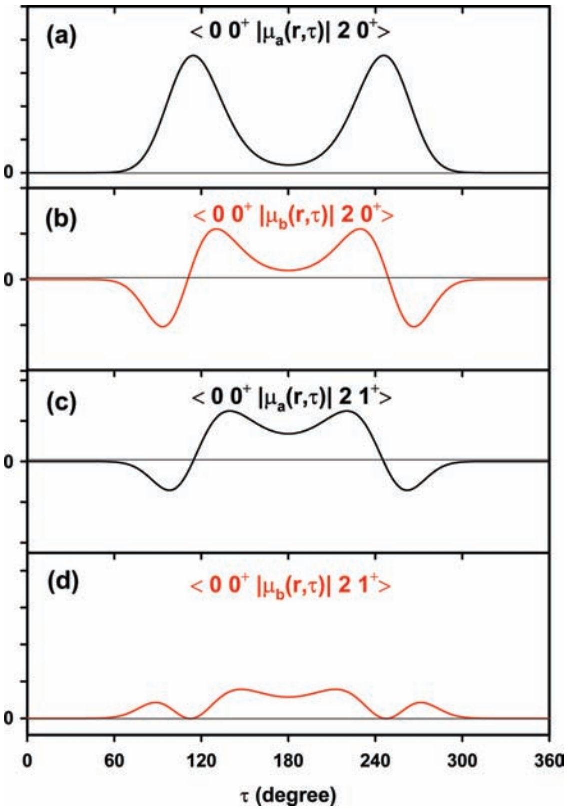

Figure 7. Transition dipole moment matrix element after integrating over just the OH stretch radial coordinate for (a) $\langle 0\ 0^+|\boldsymbol{\mu}_a(r,\tau)|2\ 0^+\rangle$; (b) $\langle 0\ 0^+|\boldsymbol{\mu}_b(r,\tau)|2\ 0^+\rangle$; (c) $\langle 0\ 0^+|\boldsymbol{\mu}_a(r,\tau)|2\ 1^+\rangle$; and (d) $\langle 0\ 0^+|\boldsymbol{\mu}_b(r,\tau)|2\ 1^+\rangle$. Note how for the $|0\ 0^+\rangle \rightarrow |2\ 0^+\rangle$ transition the integral involving $\boldsymbol{\mu}_a(\tau)$ (shown in Figure 9a) only takes on positive values, while those for $\boldsymbol{\mu}_b(\tau)$ (shown in Figure 9b) involve equal contributions from positive and negative regions. The final transition moment used to calculate the $|0\ 0^+\rangle \rightarrow |2\ 0^+\rangle$ intensity is obtained by integrating these results over the symmetric torsional wave functions involving τ. The equal contribution from the positive and negative regions makes $\boldsymbol{\mu}_b$ negligible for the $|0\ 0^+\rangle \rightarrow |2\ 0^+\rangle$ transition. Similarly the net positive contributions shown in Figure 9c and d explains why the $|0\ 0^+\rangle \rightarrow |2\ 1^+\rangle$ transition is a hybrid band involving contributions from both $\boldsymbol{\mu}_a$ and $\boldsymbol{\mu}_b$.

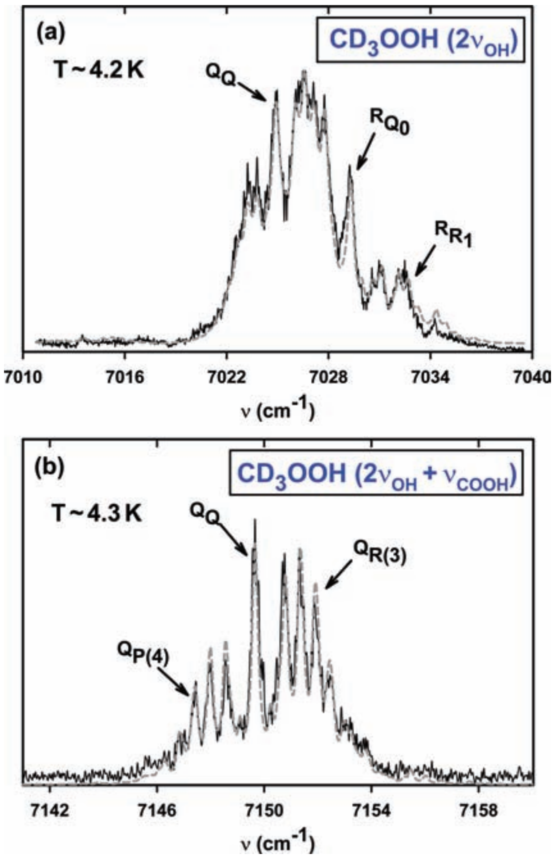

Figure 8. (a) Jet-cooled spectra of the $2\nu_{OH}$ band of CD_3OOH recorded at ~0.08 cm^{-1} resolution and 4 K obtained by probing the $OH(^2\Pi_{3/2}, v = 0)$ fragments in the $N = 5$ rotational state. On the basis of our 2-D ab initio model, the band is composed of two excitations involving the $|0\ 0^+\rangle \rightarrow |2\ 0^+\rangle$ and the $|0\ 0^+\rangle \rightarrow |2\ 0^-\rangle$ excitations. The $|0\ 0^+\rangle \rightarrow |2\ 0^+\rangle$ excitation is of pure a-type, while $|0\ 0^+\rangle \rightarrow |20^-\rangle$ is pure c-type. The overall simulation is represented by the dashed line. (b) Jet-cooled spectra of the $2\nu_{OH} + \nu_{COOH}$ combination band of CD_3OOH recorded at ~0.08 cm^{-1} resolution and 4 K. On the basis of our 2-D ab initio model, the band is composed of a single excitation involving the $|0\ 0^+\rangle \rightarrow |2\ 1^+\rangle$ transition. The rotational structure is readily discernible in both spectra.

radial coordinates "r" associated with the OH stretch, thus resulting in functions that now depend only on the torsional coordinate "τ". From Figure 7a,b, it is clear that although both of the resulting functions are symmetric about $\tau = 180°$, $\boldsymbol{\mu}_a(\tau)$ takes on strictly positive values while $\boldsymbol{\mu}_b(\tau)$ has roughly equal contributions from both positive and negative regions. Thus, when the final integration over the torsion coordinate τ is carried out using the symmetric torsional wave functions associated with the $|0\ 0^+\rangle$ and $|2\ 0^+\rangle$ states (shown in Figure 2), the result for the $\boldsymbol{\mu}_b$ matrix element ends up being 0 as the positive and negative portions of this integral just cancel each other. An analysis similar to that presented above for the $2\nu_{OH}$ band shows that the transition moment integrals associated with the $2\nu_{OH} + \nu_{COOH}$ combination band, involving the matrix elements $\langle 0\ 0^+|\boldsymbol{\mu}_a(r,\tau)|\ 2\ 1^+\rangle$ and $\langle 0\ 0^+|\boldsymbol{\mu}_b(r,\tau)|\ 2\ 1^+\rangle$, both have a net positive contribution after integrating over the radial OH stretch coordinates (see Figure 7c,d), consistent with our finding that the $2\nu_{OH} + \nu_{COOH}$ band is a hybrid band. As indicated in Table 5, we find that the $|0\ 0^+\rangle \rightarrow |2\ 1^+\rangle$ transition is a hybrid band with a $\boldsymbol{\mu}_a$ to $\boldsymbol{\mu}_b$ ratio of 1.0:0.5, very much in line with the 1:0.62 ratio predicted by the ab initio calculations.

C. Higher-Resolution Cold Spectrum of CD_3OOH $2\nu_{OH}$ and $2\nu_{OH} + \nu_{COOH}$ Bands. The above results for CH_3OOH prompted us to inquire about the potential role played by the vibrations of the methyl rotor in promoting state mixing, and we explored this issue by recording the spectra of CD_3OOH. High-resolution (~0.08 cm^{-1}) action spectra of the $2\nu_{OH}$ and $2\nu_{OH} + \nu_{COOH}$ bands in CD_3OOH recorded at 4 K are shown in Figure 8a,b. The effect of deuterium substitution is most dramatic for the combination band where the band's rotational structure is now clearly visible. To the best of our knowledge, the microwave spectrum of CD_3OOH has not been reported in the literature. Therefore, in analyzing the experimental spectra, we fixed the rotational constants for the starting $|0\ 0^+\rangle$ and $|0\ 0^-\rangle$ levels of CD_3OOH to their "expected values", which we obtained by scaling the experimental microwave rotational constants for CH_3OOH by the ratio of the ab initio rotational constants for CD_3OOH and CH_3OOH determined at the MP2/aug-cc-pVTZ level. These scaled ground-state rotational constants used in the CD_3OOH simulations are given in the lower half portion of Table 3. As with CH_3OOH, we fit the cold $2\nu_{OH}$ spectrum of CD_3OOH by taking into account the two transitions originating from the initially populated $|0\ 0^+\rangle$ level and connecting to the $|2\ 0^+\rangle$ and $|2\ 0^-\rangle$ final states. We fixed the initial-level rotational constants to the ab initio scaled values and varied the upper-state rotational constants as well as the relative weights of the transition dipole moment components. Within our resolution, the simulation gives the same effective rotational constant for both of the $|2\ 0^{+/-}\rangle$ upper states, which are $A' = 1.1077$ cm^{-1}, $B' = 0.30131$ cm^{-1}, and $C' = 0.26096$ cm^{-1}. As in the case of CH_3OOH, the rotational band types for the two excitations making up the $2\nu_{OH}$ band however are different, with the $|0\ 0^+\rangle \rightarrow |2\ 0^+\rangle$ transition being a pure a-type band while the $|0\ 0^+\rangle \rightarrow |2\ 0^-\rangle$ excitation is purely c-type. The separation between the $|2\ 0^+\rangle$ and $|2\ 0^-\rangle$ final states in CD_3OOH is ~3.54 cm^{-1}, which is slightly smaller than that in CH_3OOH. The optimized fits, shown in Figure 8a, simulate the experimental spectrum at 4 K very well, and the right half of Table 4 summarizes the optimized parameters determined for the CD_3OOH $2\nu_{OH}$ band.

Our best fit to the $2\nu_{OH} + \nu_{COOH}$ combination band of CD_3OOH is represented by the dashed lines in Figure 8b and the rotational parameters extracted for the $|2\ 1^+\rangle$ level given in the right half portion of Table 5. At 4 K, there is only a single vibration−torsion transition associated with the $|0\ 0^+\rangle \rightarrow |2\ 1^+\rangle$ excitation that contributes. The simulated spectrum again agrees very well with the results of the experiment. We find significant narrowing of the rotational line widths associated with the upper $|2\ 1^+\rangle$ state relative to their value in CH_3OOH. Specifically, these line widths are reduced from ~0.50 cm^{-1} in CH_3OOH to ~0.21 cm^{-1} in CD_3OOH. Comparing the band origins, we find that deuterium substitution has resulted in a −1.36 cm^{-1} shift for the $|0\ 0^+\rangle \rightarrow |2\ 1^+\rangle$ transition between the two isotopomers. The small magnitude of the shift is not surprising given that these vibrations do not directly involve deuterium motion (see Table 1).

D. Medium-Resolution Cold Spectra of CH_3OOH $3\nu_{OH}$ and $3\nu_{OH} + \nu_{COOH}$ Bands. Our success in analyzing the $2\nu_{OH}$ spectrum encouraged us to investigate the $3\nu_{OH}$ spectral region. On the basis of Whitten−Rabinovich algorithm, the density of vibrational states in the $3\nu_{OH}$ region is expected to be significantly higher (~2450 states/cm^{-1}) compared to that for the $2\nu_{OH}$ band (~165 states/cm^{-1}).[20] Unfortunately, it was not possible for us to generate IR light in this spectral region using difference frequency mixing; consequently, the $3\nu_{OH}$ spectra were recorded at ~0.4 cm^{-1} resolution using the MOPO laser. A cursory look at the jet-cooled spectra in Figure 5a,c suggests that $3\nu_{OH}$ and $2\nu_{OH}$ spectral regions, in many ways, look similar, with both exhibiting a strong primary band involving the OH-stretching overtone accompanied by a weaker OH stretch/COOH torsion combination band occurring slightly further to the blue. Close-ups of the $3\nu_{OH}$ and the $3\nu_{OH} + \nu_{COOH}$ bands are shown in Figure 9a and b, respectively. Looking at Figure 9a, we see that the main $3\nu_{OH}$ band at 10 267 cm^{-1} appears very congested even under jet-cooled conditions. It also exhibits a dark satellite band, which is roughly 25% of the main band intensity located toward the red at 10 255 cm^{-1} (see Figure 9a). As the temperature under which the spectrum was recorded is ~5 K, we expect only the initial $|0\ 0^+\rangle$ state to be appreciably populated. Hence, on the basis of our 2-D model, we expect only the $|0\ 0^+\rangle \rightarrow |3\ 0^+\rangle$ and $|0\ 0^+\rangle \rightarrow |3\ 0^-\rangle$ excitations to contribute to the $3\nu_{OH}$ band intensity at this temperature. Further, the ab initio model suggests that the $|0\ 0^+\rangle \rightarrow |3\ 0^-\rangle$ excitation carries ~34% of the total intensity of the $3\nu_{OH}$ band and that the separation between the $|3\ 0^+\rangle$ and the$|3\ 0^-\rangle$ final levels is expected to be less than 0.3 cm^{-1}. Thus, the two transitions $|0\ 0^+\rangle \rightarrow |3\ 0^+\rangle$ and $|0\ 0^+\rangle \rightarrow |3\ 0^-\rangle$, which primarily make up the $3\nu_{OH}$ band, are expected to be strongly overlapped. In addition, the dark state at $\nu_0 = 10\ 255$ cm^{-1}, which is unaccounted for by our simple 2-D model, also likely interacts with both the $|3\ 0^+\rangle$ and $|3\ 0^-\rangle$ final states and thus contributes to the observed broadening. Due to the lack of any discernible rotational contour, we did not attempt a simulation of the $3\nu_{OH}$ band.

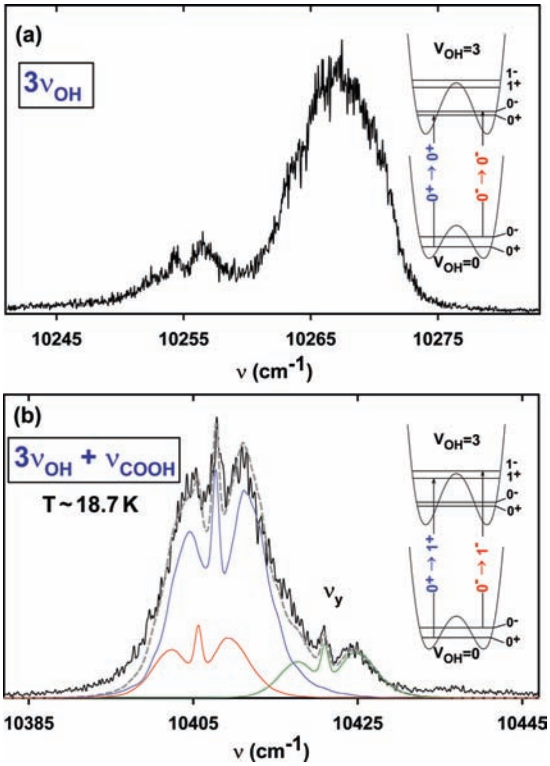

Figure 9. (a) Jet-cooled spectra of the $3\nu_{OH}$ band of CH_3OOH recorded at ~0.4 cm^{-1} resolution and 5 K obtained by probing the OH ($^2\Pi_{3/2}$, $v = 0$) fragments in the $N = 5$ rotational state. On the basis of our 2-D ab initio model, the band is composed of two nearly overlapping excitations involving the $|0\ 0^+\rangle \rightarrow |3\ 0^+\rangle$ and the $|0\ 0^+\rangle \rightarrow |3\ 0^-\rangle$ transitions. As the spectrum does not show a readily discernible rotational contour, it was not analyzed. Note the appearance of a dark state at 10 255 cm^{-1}. (b) Jet-cooled spectra of the $3\nu_{OH} + \nu_{COOH}$ combination band of CH_3OOH recorded at ~0.4 cm^{-1} resolution and 19 K. On the basis of our 2-D ab initio model, the band is primarily composed of two excitations involving the $|0\ 0^+\rangle \rightarrow |3\ 1^+\rangle$ and $|0\ 0^-\rangle \rightarrow |3\ 1^-\rangle$ transitions. The overall simulation, represented by the dashed line, also includes the dark state located at around 10 421.1 cm^{-1}.

The $3\nu_{OH} + \nu_{COOH}$ combination band shown in Figure 9b is located at ~10 408 cm^{-1}. Its rotational band contour is quite prominent and appears to be of a-type, similar to that found for the lower $2\nu_{OH} + \nu_{COOH}$ combination band. Because the $3\nu_{OH} + \nu_{COOH}$ band is relatively weak, rather modest expansion conditions were used to record its spectrum. As a result, the rotational cooling achieved corresponds to a temperature of ~19 K. Under this condition, both the $|0\ 0^+\rangle$ and $|0\ 0^-\rangle$ initial levels are expected to be appreciably populated. Hence, the vibration−torsion transitions expected to contribute toward the $3\nu_{OH} + \nu_{COOH}$ band intensity are the $|0\ 0^+\rangle \rightarrow |3\ 1^+\rangle$ and $|0\ 0^-\rangle \rightarrow |3\ 1^-\rangle$ excitations. According to the 2-D ab initio model, the separation between the final $|3\ 1^+\rangle$ and the $|3\ 1^-\rangle$ states is 27.77 cm^{-1} at $V_{OH} = 3$ (see Figure 1). Our calculations, using equations analogous to eqs 1 and 2, further suggest that the transition dipole moments associated with the $|0\ 0^+\rangle \rightarrow |3\ 1^+\rangle$ excitation will be hybrids involving both the $\boldsymbol{\mu}_a$ and $\boldsymbol{\mu}_b$ components in a ratio of 1.0:0.23, with negligible $\boldsymbol{\mu}_c$ contribution. The $|0\ 0^-\rangle \rightarrow |3\ 1^-\rangle$ transition is also expected to be a hybrid involving the $\boldsymbol{\mu}_a$ and $\boldsymbol{\mu}_b$ components in the ratio of 1.0:0.26. Finally, at 19 K, the $|0\ 0^-\rangle \rightarrow |3\ 1^-\rangle$ transition is expected to carry about a third of the intensity relative to that arising from the $|0\ 0^+\rangle \rightarrow |3\ 1^+\rangle$ excitation. Using the above information as a starting point, the simulation of the $3\nu_{OH} + \nu_{COOH}$

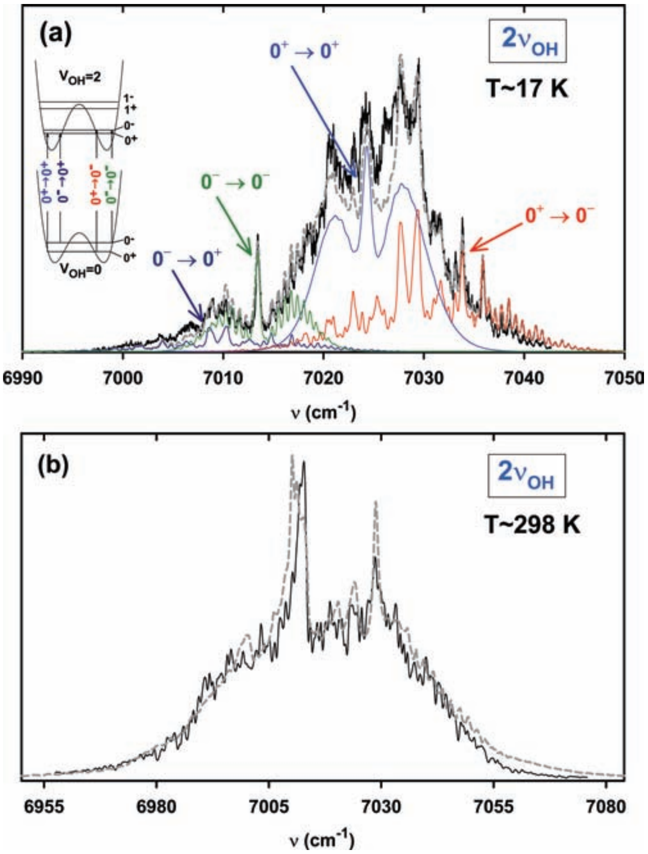

Figure 10. (a) Simulation of the CH_3OOH $2\nu_{OH}$ spectrum at 17 K. At this higher temperature, transitions originating from the 0^- torsion level must also be considered. The overall simulation, represented by the dashed lines, includes the four transitions shown. (b) Simulation of the $2\nu_{OH}$ room-temperature action spectrum.

combination band gives the best fit parameters, listed in Table 6. The corresponding simulation is represented by the dashed line in Figure 9b and consists of the sum of the $|0\ 0^+\rangle \to |3\ 1^+\rangle$ and $|0\ 0^-\rangle \to |3\ 1^-\rangle$ excitations along with an unidentified dark satellite transition, $|0\ 0^+\rangle \to |\upsilon_y{}^+\rangle$, located at 10 421.1 cm^{-1}. We note that in order to fit the $3\nu_{OH} + \nu_{COOH}$ band, the average line widths of the individual rotational transitions have to be set at 1.0 cm^{-1}, which is 2.5 times the MOPO laser line width (0.4 cm^{-1}). We did not pursue the corresponding bands of CD_3OOH due to several reasons having to do with the lack of higher resolution in this spectral region, the lower vapor pressure of CD_3OOH, as well as its significantly higher cost.

E. Simulation of Warm CH_3OOH $2\nu_{OH}$ and $3\nu_{OH} + \nu_{COOH}$ Spectra. Up to this point, we have focused primarily on transitions originating from the lowest vibration−torsion level corresponding to the $|0\ 0^+\rangle$ state. On the basis of the Boltzmann factor at 5 K, the population of the next higher torsion level, $|0\ 0^-\rangle$, is expected to be less than 1% at this temperature. In order to observe transitions originating from the higher-energy $|0\ 0^-\rangle$ level, we warmed up the free jet expansion to ~17 K by reducing the helium backing pressure. At these temperatures, the population of the $|0\ 0^-\rangle$ level is expected to increase to ~28%. The $2\nu_{OH}$ spectrum and the rotational band contours associated with this warmer expansion are shown in Figure 10a. The new sharp feature appearing at 7013.58 cm^{-1} is the band origin for the $|0\ 0^-\rangle \to |2\ 0^-\rangle$ transition. The overall band contour at 17 K, which is the sum of four vibrational transitions normalized to the relative population of their initial states, appears to capture the general experimental band shape shown in Figure 10a. The fitting parameters used in simulating the 17 K jet spectrum are given in Table 7, with only the first four columns of transitions listed, involving torsionally unexcited initial states $|0\ 0^+\rangle$ and $|0\ 0^-\rangle$, being relevant for this temperature.

Our success at simulating the jet spectra encouraged us to simulate the room-temperature spectrum of CH_3OOH in order to more closely mimic atmospheric conditions. The results for the $2\nu_{OH}$ band are shown in Figure 10b. The simulated rotational band contour for the 298 K spectrum is obtained by using the rotational constants, transition moments, and band origins for the four transitions observed in the warm 17 K jet experiments, plus two additional hot band transitions corresponding to the $|0\ 1^+\rangle \to |2\ 1^+\rangle$ and $|0\ 1^-\rangle \to |2\ 1^-\rangle$ excitations. A summary of the fitting parameters used to simulate the room-temperature spectrum is also given in Table 7, where for the 298 K simulation, all of the transitions listed contribute to the spectrum. Unlike the jet-cooled spectrum, in simulating the room-temperature spectrum, we have included the centrifugal distortion parameters Δ_K, Δ_{JK}, and Δ_J. These parameters are kept fixed to their values for the lower level given in ref 4. Analogous room-temperature simulation of the $3\nu_{OH} + \nu_{COOH}$ combination band is shown in Figure 11, with the fitting parameters listed in Table 8. A total of five vibration−torsion transitions are used in simulation of the $3\nu_{OH} + \nu_{COOH}$ band at 298 K. Of these, four are accounted for by our simple 2-D model and involve excitation from the torsional ground states corresponding to the $|0\ 0^+\rangle \to |3\ 1^+\rangle$ and $|0\ 0^-\rangle \to |3\ 1^-\rangle$ excitations as well as hot band transitions associated with the $|0\ 1^+\rangle \to |3\ 2^+\rangle$ and $|0\ 1^-\rangle \to |3\ 2^-\rangle$ excitations. Finally, the fifth transition in the $3\nu_{OH} + \nu_{COOH}$ simulation includes contribution from the dark state, which appears at around 10 421.1 cm^{-1}. The reasonable agreement between the simulations and the room-temperature action spectra in Figures 10b and 11 suggests that even though the $2\nu_{OH}$ and $3\nu_{OH} + \nu_{COOH}$ bands are perturbed, the effects of the perturbations are sufficiently small to allow us to capture the general appearance of the band contours using the rather simple approach presented.

F. IVR in CH_3OOH and CD_3OOH. Analysis of the jet-cooled spectra also allows us to glean insight into the extent of IVR in CH_3OOH, though the lack of fully resolved homogeneous structure in these measurements restricts the conclusions that we are able to reach. We find that for several states, such as $3\nu_{CH}$ and $3\nu_{OH}$, state mixing is so pervasive as to result in extensively broadened rotational contours even under jet-cooled conditions. For other states, such as $2\nu_{OH}$, $2\nu_{OH} + \nu_{COOH}$, and $3\nu_{OH} + \nu_{COOH}$, vibrational state mixing is sufficiently restricted to permit partial resolution of their rotational contours. In the discussion to follow, we primarily focus on IVR data extracted from the $2\nu_{OH}$ and $2\nu_{OH} + \nu_{COOH}$ bands, where the spectra are most resolved. To start with, as the cold temperatures associated with free jet free expansion restrict the rotational states to low *J* and *K* values in these experiments, the dark states that we see in the region of the $2\nu_{OH}$ and $2\nu_{OH} + \nu_{COOH}$ bands shown in Figure 6a,b likely arise from anharmonic coupling as opposed to Coriolis interactions. Calculations by Gai et al.[21] suggest that there are no specific anharmonic resonances that are of particular prominence in CH_3OOH. The absence of any obvious pattern of dark-state satellite peaks appearing in our overtone spectra that can be progressively tracked as one goes from the $2\nu_{OH}$ to the $3\nu_{OH}$ region and beyond (i.e., preliminary $4\nu_{OH}$ data) supports this claim. Thus, the dark satellite peaks that we do observe in the spectra (such as υ_x in Figure 6b) likely involve accidental near resonances between the zeroth-order bright state and dark bath vibrational states in the molecule. It is well-known that vibrational modes of the methyl rotor can enhance IVR.[22−24] In

TABLE 7: Spectroscopic Parameters Used to Simulate the Warm $2\nu_{OH}$ Rotational Band Contour of CH_3OOH[a]

	$|0\ 0^+\rangle \rightarrow |2\ 0^+\rangle$	$|0\ 0^+\rangle \rightarrow |2\ 0^-\rangle$	$|0\ 0^-\rangle \rightarrow |2\ 0^-\rangle$	$|0\ 0^-\rangle \rightarrow |2\ 0^+\rangle$	$|0\ 1^+\rangle \rightarrow |2\ 1^+\rangle$	$|0\ 1^-\rangle \rightarrow |2\ 1^-\rangle$
ν_0	7024.65	7028.55	7028.55	7024.65	7151.04	7192.0
$\Delta\nu$ (fwhm)	0.80	0.25	0.25	0.80	0.5	0.5
A'	1.4067	1.4067	1.4067	1.4067	1.4067	1.4067
B'	0.3480	0.3480	0.3480	0.3480	0.3480	0.3480
C'	0.3030	0.3030	0.3030	0.3030	0.3030	0.3030
$\boldsymbol{\mu}_a$	1	0	1	0	1	1
$\boldsymbol{\mu}_b$	0	0	0	0	0.50	0.50
$\boldsymbol{\mu}_c$	0	1	0	1	0	0
I[298 K][b]	1	0.7	1	0.7	0.53	0.35
I[17 K][b]	1	0.7	0.16	0.3	0	0

[a] In cm^{-1}. The transition moments are relative to the $\langle 2\ 0^+|\boldsymbol{\mu}_a|0\ 0^+\rangle$ transition. [b] Intensities are relative to the $|0\ 0^+\rangle \rightarrow |2\ 0^+\rangle$ transition.

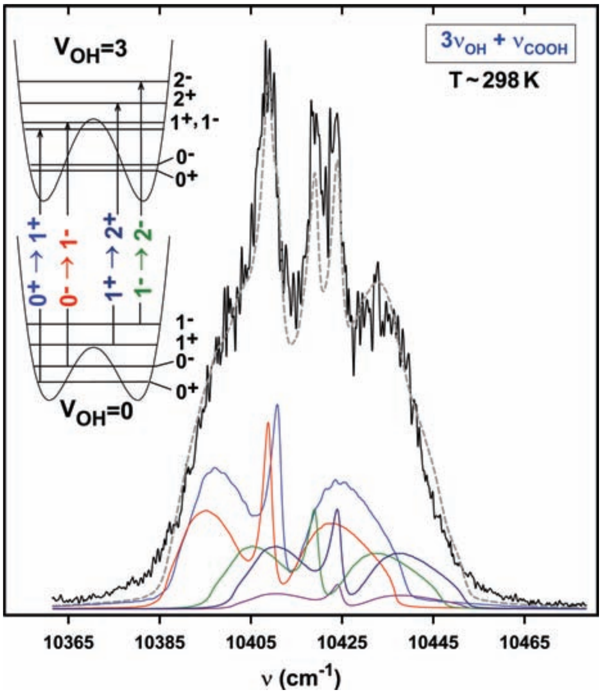

Figure 11. Simulation of the $3\nu_{OH} + \nu_{COOH}$ combination band room-temperature action spectrum. The overall simulation, represented by the dashed line, includes five transitions, four of which are accounted for by our 2-D model and are indicated on the potential energy diagram to the left. The fifth transition involves excitation to a dark state located at 10 421.1 cm^{-1}.

order to investigate the role played by these modes, we have examined the corresponding bands of the CD_3OOH isotopomer in the region of the $2\nu_{OH}$ and $2\nu_{OH} + \nu_{COOH}$ bands. Deuterium substitution at the methyl site is expected to decrease the frequencies of several vibrational modes of the molecule and hence increase the overall density of vibrational states. Using the Whitten−Rabinovich algorithm, the density of vibrational states in CH_3OOH is estimated to be ~165 states/cm^{-1} in the vicinity of the $2\nu_{OH}$ band, while for CD_3OOH, this value increases to ~581 states/cm^{-1}.[20] As shown in Table 1, deuterium substitution is also expected to significantly shift the frequency of the vibrational modes involving deuterium motion, while the frequency of the OH stretch, COOH torsion, and HOO bend remains relatively unaffected. Comparing Figures 6 and 8, we find that both the $2\nu_{OH}$ and $2\nu_{OH} + \nu_{COOH}$ bands of CD_3OOH are substantially cleaner than those of CH_3OOH, with the dark satellite features present in the CH_3OOH spectra at 7025 and 7146 cm^{-1} being absent in CD_3OOH. This observation suggests that the dark satellite features in the CH_3OOH spectra involve vibrations that shift significantly upon deuteration at the methyl site. We have attempted to provide a tentative assignment for these dark states by utilizing the fact that studies of vibrational overtones of many systems have highlighted the importance of low-order resonances in accounting for vibrational state mixing.[25,26] Among the neglected terms in the vibrational Hamiltonian, the third- and fourth-order anharmonic terms are expected to be most important as they can couple zeroth-order normal modes that differ, respectively, in a total of three and four vibrational quanta. Using experimental data for the frequency of the pure OH-stretching states in conjunction with ab initio frequencies and anharmonicities for the other modes given in Table 1, we have enumerated in Table 9 all of the vibrational states which lie within a vicinity of ±50 cm^{-1} about the bright $2\nu_{OH}$ and $2\nu_{OH} + \nu_{COOH}$ states of CH_3OOH and which differ from them by a total of three to four vibrational quanta. Of the possibilities listed, the fourth-order anharmonic resonance involving the $\nu_1 + \nu_7 + \nu_{10} + \nu_{12}$ state, which differs from the $2\nu_1$ state (i.e., $2\nu_{OH}$) by four quanta, appears to be the most reasonable choice for the dark state at 7025 cm^{-1}. This is based on its predicted relative position as well as the results of ab initio calculations presented in Table 1, which suggest that the ν_1 and ν_{12} modes exhibit significant off-diagonal anharmonicity and hence coupling in the region of the fundamental. Furthermore, its counterpart, the $\nu_1 + \nu_7 + \nu_{10} + \nu_{12} + \nu_{15}$ state, also appears to have the right separation relative to the $2\nu_1 + \nu_{15}$ (i.e., $2\nu_{OH} + \nu_{COOH}$) combination band to be identified as the dark state appearing in the CH_3OOH spectrum at 7146 cm^{-1}. This assignment however is tentative, and additional work will be required for its confirmation. As a result, we have not attempted any type of deperturbation analysis of the CH_3OOH data and defer this for future study. We point out that while ν_1 and ν_{15} correspond to the OH stretch and COOH torsion, the ν_7, ν_{10}, and ν_{12} modes, respectively, correspond to the CH_3 umbrella, CH_3 rock, and OO stretch.

In addition to the dark satellite features arising from strong coupling, the presence of weaker intramolecular interactions is reflected in the broadening of individual rovibrational transitions. In the tier model description of IVR, these weaker interactions arise from indirect coupling of the bright state with dark bath states associated with the second and higher tiers.[25,26] In order to obtain reasonable fits to the jet-cooled $2\nu_{OH}$ band of CH_3OOH, we found it necessary to use ~0.7 cm^{-1} wide (fwhm) Lorentzian line shapes for the rotational transitions associated with the $|2\ 0^+\rangle$ level and a width of 0.25 cm^{-1} for the $|2\ 0^-\rangle$ level. Deconvoluting out the 0.08 cm^{-1} resolution of our IR laser results in widths that are, respectively, 0.695 and 0.237 cm^{-1}. As the $2\nu_{OH}$ excitation energy is far below the dissociation threshold, this broadening is not due to unimolecular dissociation reducing the lifetime of the states but arises from state mixing in the upper vibrational level. It is interesting that the rotational line width for the $|2\ 0^+\rangle$ state is found to be larger than those of

TABLE 8: Spectroscopic Parameters Used to Simulate the Warm $3\nu_{OH} + \nu_{COOH}$ Rotational Band Contour of CH_3OOH at 298 K[a]

	$|0\ 0^+\rangle \rightarrow |3\ 1^+\rangle$	$|0\ 0^-\rangle \rightarrow |3\ 1^-\rangle$	$|0\ 1^+\rangle \rightarrow |3\ 2^+\rangle$	$|0\ 1^-\rangle \rightarrow |3\ 2^-\rangle$	$|0\ 1^+\rangle \rightarrow |v_y{}^+\rangle$
ν_0	10 407.85	10 420.65	10 551.0	10 607.0	10 421.1
$\Delta\nu$ (fwhm)	1.0	1.0	1.0	1.0	1.0
A'	1.4140	1.4140	1.4140	1.4140	1.4140
B'	0.3562	0.3562	0.3562	0.3562	0.3562
C'	0.3062	0.3062	0.3062	0.3062	0.3062
$\boldsymbol{\mu}_a$	1	1	1	0	1
$\boldsymbol{\mu}_b$	0.23	0.26	0.23	0.23	0.23
$\boldsymbol{\mu}_c$	0	0	0	0	0
I^b	1	0.94	0.5	0.45	0.20

[a] In cm^{-1}. The transition moments are relative to the $\langle 3\ 1^+|\boldsymbol{\mu}_a|0\ 0^+\rangle$ transition. [b] Intensities are relative to the $|0\ 0^+\rangle \rightarrow |3\ 1^+\rangle$ transition.

TABLE 9: States within ±50 cm^{-1} of $2\nu_1$ and $2\nu_1 + \nu_{15}$ That Can Couple to Them through Anharmonic Interactions[a]

	$2\nu_1$ state	$2\nu_1 + \nu_{15}$ state
third-order interactions	$\nu_1 + \nu_2 + \nu_{13}$ (+42.3)	$\nu_1 + \nu_2 + \nu_{13} + \nu_{15}$ (+32.9)
	$\nu_1 + \nu_3 + \nu_{13}$ (+11.5)	$\nu_1 + \nu_3 + \nu_{13} + \nu_{15}$ (−2.4)
	$\nu_1 + \nu_4 + \nu_{13}$ (−50.4)	
forth-order interactions	$\nu_1 + \nu_2 + \nu_{14} + \nu_{15}$ (−37.6)	$\nu_1 + \nu_2 + \nu_{14} + 2\nu_{15}$ (−47.7)
	$\nu_1 + \nu_4 + 2\nu_{14}$ (−12.6)	$\nu_1 + \nu_3 + 2\nu_{14} + \nu_{15}$ (+33.4)
	$\nu_1 + \nu_5 + \nu_{10} + \nu_{12}$ (+48.4)	$\nu_1 + \nu_4 + 2\nu_{14} + \nu_{15}$ (−27.4)
	$\nu_1 + 2\nu_5 + \nu_{13}$ (−27.7)	$\nu_1 + \nu_5 + \nu_{10} + \nu_{12} + \nu_{15}$ (+41.7)
	$\nu_1 + \nu_6 + \nu_9 + \nu_{12}$ (+29.5)	$\nu_1 + 2\nu_5 + \nu_{13} + \nu_{15}$ (−38.6)
	$\nu_1 + \nu_6 + \nu_{10} + \nu_{12}$ (+8.0)	$\nu_1 + \nu_6 + \nu_9 + \nu_{12} + \nu_{15}$ (+32.8)
	$\nu_1 + \nu_7 + \nu_9 + \nu_{12}$ (12.7)	$\nu_1 + \nu_6 + \nu_{10} + \nu_{12} + \nu_{15}$ (−0.1)
	$\nu_1 + \nu_7 + \nu_{10} + \nu_{12}$ (−0.7)	$\nu_1 + \nu_7 + \nu_9 + \nu_{12} + \nu_{15}$ (+17.1)
	$\nu_1 + \nu_7 + 2\nu_{11}$ (+37.8)	$\nu_1 + \nu_7 + \nu_{10} + \nu_{12} + \nu_{15}$ (−7.6)
	$\nu_1 + 3\nu_{10}$ (+27.2)	$\nu_1 + \nu_7 + 2\nu_{11} + \nu_{15}$ (+44.5)
		$\nu_1 + 2\nu_8 + \nu_{12} + \nu_{15}$ (+34.6)
		$\nu_1 + 2\nu_9 + \nu_{11} + \nu_{15}$ (−36.4)
		$\nu_1 + 3\nu_{10} + \nu_{15}$ (+22.2)

[a] Values in parentheses indicate the position relative to the bright state band (in cm^{-1}).

$|2\ 0^-\rangle$ in both CH_3OOH and CD_3OOH (see Table 4). This difference likely reflects variation in IVR rates for these vibrational states, although slight differences in rotational structure associated with the unresolved A/E states, arising from the methyl torsion, may also be contributing.[4] From an analysis of the $2\nu_{OH} + \nu_{COOH}$ combination band spectrum, we find that rotational transitions to the $|2\ 1^+\rangle$ state have an average deconvoluted width of ~0.494 cm^{-1} in CH_3OOH and 0.194 cm^{-1} in CD_3OOH (fwhm). The fact that the widths for the CD_3OOH $|2\ 1^+\rangle$ state are narrower, even though the vibrational state density is ~3.5 times higher, is consistent with the idea that IVR rates are typically determined by specific coupling to a small subset of background states and not just overall vibrational state densities.[25,26] The 0.194 cm^{-1} width associated with the CD_3OOH $|2\ 1^+\rangle$ combination band gives an upper limit for the time scale for energy flow out of the zeroth-order bright state, if it were excited coherently, and into the dense background bath states of $\tau \geq 27$ ps ($\tau \approx 1/2\pi c\Delta\nu$). By contrast, the time scale for initial energy flow out of the corresponding $|2\ 1^+\rangle$ state of CH_3OOH is given by the 5 cm^{-1} separation between the dark-state feature at 7146 cm^{-1} and the main band at 7151 cm^{-1} and corresponds to ~1 ps. In addition, in both CH_3OOH and CD_3OOH, the rotational line width of the combination mode $|2\ 1^+\rangle$ is measured to be narrower than those of the $|2\ 0^+\rangle$ state, suggesting that the rate for energy dissipation from the zero-order state into the dense bath modes does not increase when a quanta of COOH torsion is added to the OH-stretching overtone. This finding is in contrast to that observed in hydrogen peroxide, where higher IVR rates were found for the $6\nu_{OH+HOOH}$ stretch−torsion combination compared to that for the pure $6\nu_{OH}$ stretching state.[27]

IV. Conclusion

The spectral regions corresponding to the first and second OH-stretching overtones in CH_3OOH have been examined under free jet expansion conditions using action spectroscopy. By recording the spectra under higher resolution and colder temperatures than in our previous work, we have been able to partially resolve the rotational structures for several vibrational bands and hence determine the orientation of their transition dipole moment as well as effective spectroscopic constants. In addition, a closer examination of the bands has revealed evidence of dark states arising from vibrational state mixing. Our findings suggest that the simple 2-D ab initio vibration−torsion model can successfully predict several aspects of the OH overtone spectra, including relative intensity and transition dipole moment orientation. Not surprisingly, the model fails to account for dark states appearing in the experimental spectra. The role of the methyl rotor in promoting IVR in the lower OH-stretching overtone and combination bands of CH_3OOH and CD_3OOH has been examined. These first results show that state mixing in the $2\nu_{OH}$ and $2\nu_{OH} + \nu_{COOH}$ bands of CH_3OOH are much more extensive than that in CD_3OOH, and the extent of rotational structure in the bands allows us to place limits on the IVR decay rates. Spectroscopic studies of large-amplitude motion in CH_3OOH and its influence on IVR complements the studies on CH_3OH[28−30] as the proximity of the methyl rotor relative to the OH group is different in the two systems. Future studies using double resonance should provide additional simplification and insight into the dynamics of state mixing in CH_3OOH. From a practical perspective, the spectroscopic parameters gleaned from the present study should be useful in modeling atmospheric absorption profiles of methyl hydroperoxide and its temperature dependence in the infrared.

Acknowledgment. Funding for this work was provided by a grant from the National Science Foundation (CHE-0642640).

References and Notes

(1) Brasseur, G. P.; Orlando, J. J.; Tyndall, G. S. *Atmospheric Chemistry and Global Change*; Oxford University Press: New York, 1999.

(2) Sander, S. P.; Friedl, R. R.; Golden, D. M.; Kurylo, M. J.; Huie, R. E.; Orkin, V. L.; Moortgat, G. K.; Ravishankara, A. R.; Kolb, C. E.; Molina, M. J.; Finlayson-Pitts, B. J. *Chemical Kinetics and Photochemical Data for use in Stratospheric Modeling*; Evaluation #14; JPL Publ.: 02-25; **2003**.

(3) Finlayson-Pitts, B. J.; Pitts, J. N., Jr. *Atmospheric Chemistry: Fundamental and Experimental Techniques*; Wiley: New York, 1986.

(4) Tyblewski, M.; Ha, T.-K.; Meyer, R.; Bauder, A.; Blom, C. E. *J. Chem. Phys.* **1992**, *97*, 6168.

(5) Homitsky, S. C.; Dragulin, S. M.; Haynes, L. M.; Hsieh, S. *J. Phys. Chem. A* **2004**, *108*, 9492.

(6) (a) Haynes, L. M.; Vogelhuber, K. M.; Pippin, J. L.; Hsieh, S. *J. Chem. Phys.* **2005**, *123*, 234306. (b) Erratum, *J. Chem. Phys.* **2007**, *126*, 209901.

(7) Matthews, J.; Martínez-Avilés, M.; Francisco, J. S.; Sinha, A. *J. Chem. Phys.* **2008**, *129*, 074316.

(8) Dübal, H. R.; Crim, F. F. *J. Chem. Phys.* **1985**, *83*, 3863.

(9) Likar, M. D.; Baggott, J. E.; Crim, F. F. *J. Chem. Phys.* **1989**, *90*, 6266.

(10) Sage, M. L.; Jortner, J. *Adv. Chem. Phys.* **1981**, *47*, 293.

(11) Dutton, G.; Barnes, R. J.; Sinha, A. *J. Chem. Phys.* **1999**, *111*, 4976.

(12) Rothman, L. S.; Barbe, A.; Chris Benner, D.; Brown, L. R.; Camy-Peyret, C.; Carleer, M. R.; Chance, K.; Clerbaux, C.; Dana, V.; Devi, V. M.; Fayt, A.; Flaud, J.-M.; Gamache, R. R.; Goldman, A.; Jacquemart, D.; Jucks, K. W.; Lafferty, W. J.; Mandin, J.-Y.; Massie, S. T.; Nemtchinov, V.; Newnham, D. A.; Perrin, A.; Rinsland, C. P.; Schroeder, J.; Smith, K. M.; Smith, M. A. H.; Tang, K.; Toth, R. A.; Vander Auwera, J.; Varanasi, P.; Yoshino, K. *J. Quantum Spectrosc. Radiat. Transfer* **2003**, *82*, 5.

(13) Vaghjiani, G. L.; Ravishankara, A. R. *J. Geophys. Res.* **1989**, *94*, 3487.

(14) Western, C. M. PGOPHER, version 5.2.343, a program for simulating rotational structure; University of Bristol: Bristol, U.K.; http://pgopher.chm.bris.ac.uk.

(15) Fair, J. R.; Votava, O.; Nesbitt, D. J. *J. Chem. Phys.* **1998**, *108*, 72.

(16) Konen, I. M.; Pollack, I. B.; Li, E. X. J.; Lester, M. I.; Varner, M. E.; Stanton, J. F. *J. Chem. Phys.* **2005**, *122*, 94320.

(17) Weinhold, F.; Landis, C. R. *Valency and Bonding: A Natural Bond Orbital Donor−Acceptor Perspective*; Cambridge University Press: Cambridge, U.K., 2003.

(18) (a) Carpenter, J. E.; Weinhold, F. *J. Phys. Chem.* **1988**, *92*, 4295. (b) Carpenter, J. E.; Weinhold, F. *J. Phys. Chem.* **1988**, *92*, 4306.

(19) Hernández-Soto, H.; Weinhold, F.; Francisco, J. S. *J. Chem. Phys.* **2007**, *127*, 164102.

(20) Holbrook, K. A.; Pilling, M. J.; Robertson, S. H. *Unimolecular Reactions*, 2nd ed.; Wiley: New York, 1996.

(21) Gai, H.; Thompson, D. L.; Fisk, G. A. *J. Chem. Phys.* **1989**, *90*, 7055.

(22) Parmenter, C. S.; Stone, B. M. *J. Chem. Phys.* **1986**, *84*, 4710.

(23) Bethardy, G. A.; Wang, X. L.; Perry, D. S. *Can. J. Chem.* **1994**, *72*, 652.

(24) Perry, D. S.; Bethardy, G. A.; Wang, X. L. *Ber. Bunsen Ges.* **1995**, *99*, 530.

(25) Nesbitt, D. J.; Field, R. W. *J. Phys. Chem.* **1996**, *100*, 12735.

(26) Lehmann, K. K.; Scoles, G.; Pate, B. H. *Annu. Rev. Phys. Chem.* **1994**, *45*, 241.

(27) Kuhn, B.; Rizzo, T. R. *J. Chem. Phys.* **2000**, *112*, 7461.

(28) Boyarkin, O. V.; Lubich, L.; Settle, R. D. F.; Perry, D. S.; Rizzo, T. R. *J. Chem. Phys.* **1997**, *107*, 8409.

(29) (a) Boyarkin, O. V.; Rizzo, T. R.; Perry, D. S. *J. Chem. Phys.* **1999**, *110*, 11346. (b) Boyarkin, O. V.; Rizzo, T. R.; Perry, D. S. *J. Chem. Phys.* **1999**, *110*, 11359.

(30) Chirokolava, A.; Perry, D. S.; Boyarkin, O. V.; Schmid, M.; Rizzo, T. R. *J. Chem. Phys.* **2000**, *113*, 10068.

JP902146Z